Turbulent reconnection of magnetic bipoles in stratified turbulence

S. Jabbari[1,2] *, A. Brandenburg[1,2,3,4], Dhrubaditya Mitra[1], N. Kleeorin [5,1], I. Rogachevskii [5,1]

[1]*Nordita, KTH Royal Institute of Technology and Stockholm University, Roslagstullsbacken 23, SE-10691 Stockholm, Sweden*
[2]*Department of Astronomy, AlbaNova University Center, Stockholm University, SE-10691 Stockholm, Sweden*
[3]*JILA and Department of Astrophysical and Planetary Sciences, Box 440, University of Colorado, Boulder, CO 80303, USA*
[4]*Laboratory for Atmospheric and Space Physics, 3665 Discovery Drive, Boulder, CO 80303, USA*
[5]*Department of Mechanical Engineering, Ben-Gurion University of the Negev, POB 653, Beer-Sheva 84105, Israel*

ABSTRACT
We consider strongly stratified forced turbulence in a plane-parallel layer with helicity and corresponding large-scale dynamo action in the lower part and non-helical turbulence in the upper. The magnetic field is found to develop strongly concentrated bipolar structures near the surface. They form elongated bands with a sharp interface between opposite polarities. Unlike earlier experiments with imposed magnetic field, the inclusion of rotation does not strongly suppress the formation of these structures. We perform a systematic numerical study of this phenomenon by varying magnetic Reynolds number, scale separation ratio, and Coriolis number. We focus on the formation of a current sheet between bipolar regions where reconnection of oppositely oriented field lines occurs. We determine the reconnection rate by measuring either the inflow velocity in the vicinity of the current sheet or by measuring the electric field in the reconnection region. We demonstrate that for large Lundquist numbers, $S > 10^3$, the reconnection rate is nearly independent of S in agreement with results of recent numerical simulations performed by other groups in simpler settings.

Key words: Magnetohydrodynamics - turbulence - Sun: sunspots - dynamo

1 INTRODUCTION

The mechanism for the formation of sunspots and active regions is still not understood. One popular model assumes that the solar dynamo generates thin, strong magnetic flux tubes of $\sim 10^5$ G near the tachocline (D'Silva & Choudhuri 1993). Part of these tubes can become magnetically buoyant and rise to the surface creating sunspots and active regions (Parker 1955; Choudhuri et al. 1995); see also Fan (2009) for a review. So far neither numerical (Guerrero & Käpylä 2011) nor observational (Fan 2009; Zhao et al. 2013; Getling et al. 2016) studies have confirmed this scenario. Furthermore, the flux tubes are expected to expand as they rise, hence their strength weakens and some sort of re-amplification mechanism must complement this model to match the observational properties of sunspots.

An alternative mechanism for the formation of active regions and sunspots is based on the negative effective (mean-field) magnetic pressure instability (NEMPI). Analytical studies (Kleeorin et al. 1989, 1990, 1993, 1996; Kleeorin & Rogachevskii 1994; Rogachevskii & Kleeorin 2007) supported by direct numerical simulations (Brandenburg et al. 2012; Käpylä et al. 2012, 2016) have shown that in stratified turbulence in the presence of a background magnetic field the effective magnetic pressure (the sum of turbulent

and non-turbulent contributions) can become negative. This effect can give rise to a large-scale instability (Rogachevskii & Kleeorin 2007; Kemel et al. 2013), i.e., NEMPI, which can lead to the concentration of a weak background magnetic field. Once the field becomes strong enough – more than the local equipartition value – the effective magnetic pressure is no longer negative and NEMPI is not excited. Direct numerical simulations (DNS) of stratified turbulence have demonstrated that NEMPI can produce magnetic field concentrations (Brandenburg et al. 2010, 2011; Kemel et al. 2013; Jabbari et al. 2014) from background magnetic fields that can be either perpendicular or parallel to the density gradient in both spherical and rectangular domains. In the latter case, spot-like structures near the surface (Brandenburg et al. 2013, 2014) are obtained. A further generalization to a two-layer model (Warnecke et al. 2013, 2016) with non-helical forcing in the lower layer and no forcing in the upper has been successful in generating bipolar magnetic structures with intriguing dynamical behavior. Furthermore, mean-field simulations have shown that the concentration of a background magnetic field by NEMPI can operate even in the presence of dynamo action (Jabbari et al. 2013).

Nevertheless, there are two limitations to the aforementioned studies: (a) it is necessary to have a weak initial background magnetic field to excite NEMPI, and (b) the maximum strength of the magnetic field in the nonlinear stage of NEMPI can be at most three times larger than the local equipartition value. Mitra et al.

* E-mail: sarahjab@kth.se

(2014) and Jabbari et al. (2015) have circumvented these limitations respectively in their Cartesian and spherical models by using a two-layer arrangement of forced stratified turbulence in which the bottom layer is helically forced and the top layer is non-helically forced. In both of these cases, a large-scale dynamo develops in the bottom layer and provides a background magnetic field that is concentrated by stratified turbulence in the top layer to generate intense magnetic structures of strengths that can be close to five times the equipartition value. It is not clear that NEMPI is the relevant mechanism that gives rise to the magnetic structures observed by Mitra et al. (2014) or Jabbari et al. (2015). Although Mitra et al. (2014) have not measured the effective magnetic pressure, they did detect large-scale downflows at the location of the magnetic flux concentrations. Similar downflows have been found previously in forced turbulence with an imposed vertical field (Brandenburg et al. 2013, 2014), where NEMPI was found to lead to magnetic spot formation. In the work of Jabbari et al. (2015), NEMPI could only be excited in those parts of the domain where the strength of the dynamo-generated field was sufficiently below the equipartition magnetic field. Nevertheless, also in that case formation of spots coincided with downflows.

The purpose of the present study is two-fold. On the one hand, using the model of Mitra et al. (2014), we perform a systematic numerical study of the formation and decay of bipolar regions by varying different parameters of the problem, in particular the magnetic Reynolds number and the scale separation ratio. Furthermore, we study the effects of rotation through the Coriolis term in the same model. As emphasized by Mitra et al. (2014) and Jabbari et al. (2015), the lifetime of the sharp interface between the bipolar regions is much longer than what one estimates from the effects of turbulent diffusion. This suggests that the sharp interface is constantly being maintained by converging flows, which lead to the formation of a current sheet between two polarities and the occurrence of turbulent reconnection.

Magnetic reconnection is a fundamental plasma process that is believed to play an important role in different astrophysical, geophysical, and laboratory plasma phenomena, e.g., solar flares, coronal mass ejections, coronal heating, magnetospheric substorms and tearing mode instabilities in magnetic confinement fusion devices (Priest 2014; Zweibel & Yamada 2009; Loureiro et al. 2013). A classical model of reconnection was suggested by Parker (1957) and Sweet (1958); see also their later works (Sweet 1969; Parker 1994). According to the Sweet-Parker model, the reconnection rate is proportional to the square root of the magnetic diffusivity of the plasma. This would imply that in the astrophysically relevant limit of very small magnetic diffusivity (or very large Lundquist number) the Sweet-Parker reconnection rate would go to zero. Hence, for reconnection to be relevant in the astrophysical context it is necessary to find models of fast reconnection in which the reconnection rate is independent of Lundquist number in the asymptotic limit of large Lundquist number. Recently, fast reconnection has been studied in DNS of turbulent magnetohydrodynamics (MHD) in both two and three dimensions (Loureiro et al. 2009; Kowal et al. 2009; Huang & Bhattacharjee 2010; Loureiro et al. 2012; Beresnyak 2013; Oishi et al. 2015), and at least two competing models: by Lazarian & Vishniac (1999); Eyink et al. (2011) and by Uzdensky et al. (2010); Loureiro et al. (2013) have been proposed, see, e.g., Lazarian et al. (2015) for a review. To investigate the role of magnetic reconnection in our model, we zoom in on the flow around the sharp interface, study the dynamics of the current sheet in this region and measure the reconnection rate to determine which regime of turbulent reconnection is relevant to our system.

2   THE MODEL

2.1   Basic equations

To perform DNS of an isothermally stratified layer, we solve the equations for the velocity U, the magnetic vector potential A, and the density ρ and, in some cases, also in the presence of nonvanishing angular velocity $\boldsymbol{\Omega} = \Omega \hat{\boldsymbol{z}}$,

$$\rho \frac{\mathrm{D}U}{\mathrm{D}t} = J \times B - 2\boldsymbol{\Omega} \times \rho U - c_{\mathrm{s}}^2 \boldsymbol{\nabla} \rho + \boldsymbol{\nabla} \cdot (2\nu\rho \mathsf{S}) + \rho(\boldsymbol{f} + \boldsymbol{g}), \quad (1)$$

$$\frac{\partial A}{\partial t} = U \times B + \eta \nabla^2 A, \quad (2)$$

$$\frac{\partial \rho}{\partial t} = -\boldsymbol{\nabla} \cdot \rho U, \quad (3)$$

where the operator $\mathrm{D}/\mathrm{D}t = \partial/\partial t + U \cdot \boldsymbol{\nabla}$ is the advective derivative, $\mathsf{S}_{ij} = \frac{1}{2}(U_{i,j} + U_{j,i}) - \frac{1}{3}\delta_{ij}\boldsymbol{\nabla} \cdot U$ is the traceless rate of strain tensor (the commas denote partial differentiation), ν is the kinematic viscosity, c_{s} is the isothermal sound speed, μ_0 is the vacuum permeability, η is the magnetic diffusivity, $B = \nabla \times A$ is the magnetic field, and $J = \nabla \times B/\mu_0$ is the current density.

We perform simulations in a cubic domain of size L^3. This implies that the smallest wavenumber which fits into the box is 1 ($k_1 = 2\pi/L = 1$). We apply the same boundary condition as Mitra et al. (2014), i.e., we use periodic boundary conditions in the x and y directions, stress-free perfect conductor boundary conditions at the bottom of the domain, ($z = -L/2$) and stress-free vertical field conditions at the top ($z = +L/2$).

The stratification is isothermal with constant gravity given by $\boldsymbol{g} = (0, 0, -g)$, so the density scale height is $H_\rho = c_{\mathrm{s}}^2/g$. In all the cases considered below we have $k_1 H_\rho = 1$ and $L/H_\rho = 2\pi$. In this setup the density contrast across the domain is $\exp(L_z/H_\rho) = \exp 2\pi \approx 535$. Since we have adopted an isothermal equation of state, there is no possibility of convection. We apply random volume forcing to drive turbulence. It is defined by a function f that is δ-correlated in time and monochromatic in space. It consists of random non-polarized waves whose direction and phase change randomly at each time step. To simulate the two-layer model of Mitra et al. (2014), we define the forcing profile such that we have helical forcing in the lower part of the domain ($z < z_\star$) and non-helical forcing in the upper ($z > z_\star$). Here, $z_\star$ is the position of the border between helical and non-helical forcing; in our model we choose $z_\star = -H_\rho$. The helical forcing leads to the generation of a large-scale magnetic field in the lower layer due to α^2 dynamo action. The field then diffuses to the upper layer where the magnetic bipolar spots are expected to form. For more details regarding the forcing profile, see Mitra et al. (2014).

This setup is chosen to demonstrate the physical effects in isolation. In particular, the region of the dynamo generating large-scale weakly non-uniform magnetic field is separated from the region where the strongly non-uniform bipolar magnetic region is formed. This arrangement can also mimic a nonuniform spatial distribution of kinetic helicity and α effect in the solar convective zone, e.g., the α is larger in the deeper parts of the convective zone (Krivodubskii 1984).

Table 1. Summary of the runs. The reference run is shown in bold.

Run	$\mathrm{Re_M}$	k_f/k_1	$z_\star/H_\rho$	$\lambda/\eta_{t0}k_1^2$
D	16	30	-1	0.042
RM0	10	30	-1	0.05
RM1	**50**	**30**	**-1**	**0.014**
RM1zs	50	30	π	0.013
RM1k	50	5	-1	0.024
RM2	130	30	-1	0.005
RM3	260	30	-1	0.002
RM4	300	30	-1	0.001

2.2 Parameters of the simulations

To solve Eqs. (1)–(3), we perform DNS with the PENCIL CODE[1]. It uses sixth-order explicit finite differences in space and a third-order accurate time-stepping method. We use a numerical resolution of $256 \times 252 \times 256$ mesh points in the x, y, and z directions. We choose our units such that $c_s = g = \mu_0 = 1$. Our simulations are characterized by the fluid Reynolds number, $\mathrm{Re} \equiv u_{\mathrm{rms}}/\nu k_f$, and the magnetic Prandtl number, $\mathrm{Pr_M} = \nu/\eta$, so the magnetic Reynolds number is $\mathrm{Re_M} \equiv \mathrm{Re}\,\mathrm{Pr_M} = u_{\mathrm{rms}}/\eta k_f$. Here, k_f/k_1 is the forcing wavenumber, which takes a value of 30 in most of our simulations. We also study the case $k_f/k_1 = 5$. In all runs we keep, $\mathrm{Pr_M} = 0.5$ and vary $\mathrm{Re_M}$.

As the value of the turbulent velocity is set by the local strength of the forcing, which is uniform, the turbulent velocity is also statistically uniform over depth, and therefore we choose to define u_{rms} as the root-mean-square velocity based on a volume average in the statistically steady state. On the other hand, the density varies over several orders of magnitude as a function of depth and hence we define the mean density $\overline{\rho}$ as a a horizontally and temporally averaged density at each depth. The magnetic field is expressed in units of the local equipartition value, $B_{\mathrm{eq}} \equiv \sqrt{\mu_0 \overline{\rho}}\, u_{\mathrm{rms}}$. Time is measured in turbulent-diffusive times, $\tau_{\mathrm{td}} = (\eta_{t0} k_1^2)^{-1}$, where $\eta_{t0} = u_{\mathrm{rms}}/3k_f$ is the estimated turbulent magnetic diffusivity.

Most of the parameters are similar to those of Mitra et al. (2014), but we vary $\mathrm{Re_M}$ and also consider cases with rotation. We also study the effect of the scale separation ratio, k_f/k_1, by changing k_f to investigate its effect on the formation and evolution of bipolar structures. Table 1 shows all runs with their parameters.

We characterize the reconnection of the bipolar magnetic structures by the Lundquist number, S:

$$S = V_A \mathcal{L}/\eta, \tag{4}$$

where $V_A = B/\sqrt{\mu_0 \rho}$ is the Alfvén velocity, and $\mathcal{L}$ is a typical length scale, which is here taken to be the length of the current sheet.

3 PROPERTIES OF THE DYNAMO

The magnetic field in our model is the result of a large-scale dynamo. We recall that the forcing in the momentum equation is fully helical in the lower 30% of the box and non-helical in the rest. We expect that the α^2 dynamo generates an exponentially growing magnetic field during the early phase when the field is weak.
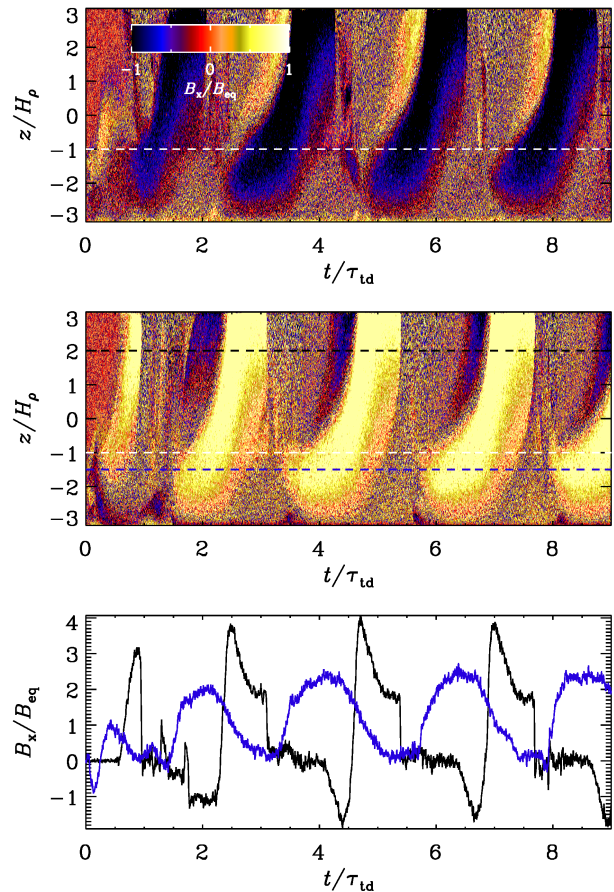
Figure 1. Butterfly diagrams $B(x_c, y_c, z, t)/B_{\mathrm{eq}}(z)$ for Run RM1 through cross-sections $x_c/H_\rho = \pi$, and either $y_c/H_\rho = 1.8$ (top panel) or -1.8 (middle panel), as well as $B_x(x_c, y_c, z_c, t)/B_{\mathrm{eq}}$ through $x_c/H_\rho = \pi$, $y_c/H_\rho = -1.8$, for both $z_c/H_\rho = 2$ (black line) and $z_c/H_\rho = -1.5$ (blue line) versus time (lower panel). The white dashed lines in the upper two panels indicate the position of $z_\star$ and in the second panel the dashed blue and black horizontal lines show the locations where $B_x(x_c, y_c, z_c, t)/B_{\mathrm{eq}}$ is plotted vs. t.

The dynamo-generated field has a periodic behavior with dynamo waves propagating in the deeper part of the domain, where the forcing is helical ($z/H_\rho < -1$). To study the dynamo properties, we plot the butterfly diagram in Fig. 1. The upper panel shows the butterfly diagram at $y/H_\rho = 1.8$ and the middle panel presents the same plot for $y/H_\rho = -1.8$. The upward speed of the pattern increases as one moves toward the surface. The nondimensional growth rate is given as $\tilde{\lambda} = \lambda/u_{\mathrm{rms}} k_f$, where $\lambda = \mathrm{d} \ln B_{\mathrm{rms}}/\mathrm{d}t$, and its value decreases with increasing magnetic Reynolds number (see Table 1 and the lower panel of Fig. 2). The large-scale magnetic field expands upward into the region with non-helical forcing due to turbulent magnetic diffusion. In this region, density is lower, so the field strongly exceeds the equipartition value. Here the field evolution is highly nonlinear and driven by the dynamo wave from beneath.

To measure the period of the dynamo cycle, we plot in the lower panel of Fig. 1 the value of B_x/B_{eq} as a function of time for two different depths, $z/H_\rho = -1.5$ (inside the helical region; blue curve) and $z/H_\rho = 2$ (near the surface; black curve). In Run D the value of the period is about $1.6\tau_{\mathrm{td}}$ for $\mathrm{Re_M} = 16$. This is consistent
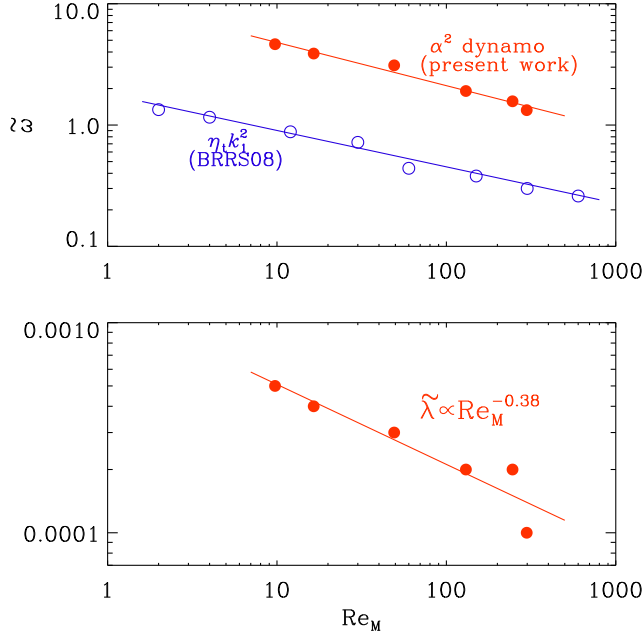
Figure 2. Upper panel: normalized dynamo frequency, $\tilde{\omega}$, as a function of Re_M. The solid lines show the best fit to our data points (red closed circles) and the data points of Brandenburg et al. (2008) (blue open circles). Lower panel: normalized growth rate of dynamo, $\tilde{\lambda}$, as a function of Re_M. The solid line shows the best fit to our data points.

with the result of Mitra et al. (2014), where a period of the dynamo wave of $1.5\tau_{\mathrm{td}}$ was determined.

In the upper panel of Fig. 2 we show the dependence of the normalized dynamo frequency, $\tilde{\omega} = \omega/\eta_{\mathrm{t}0}k_1^2$, on the magnetic Reynolds number, Re_M. The fit overplotted on the data has the form

$$\tilde{\omega} \approx 11\,\mathrm{Re}_\mathrm{M}^{-0.36}. \qquad (5)$$

Although the large-scale dynamo that develops in this problem is an α^2 dynamo, the functional dependence of ω on Re_M is similar to that of a nonlinear $\alpha\Omega$ dynamo in a Cartesian domain with linear shear (Käpylä & Brandenburg 2009). In that case, $\omega \propto \eta_{\mathrm{t}}k_1^2$ is proportional to the quenched turbulent magnetic diffusivity, η_{t}. In a separate study of a nonlinear α^2 dynamo, the quenched values of η_{t} were found to be proportional to $\mathrm{Re}_\mathrm{M}^{-0.3}$ for $2 \leqslant \mathrm{Re}_\mathrm{M} \leqslant 600$ (Brandenburg et al. 2008). The scaling of the resulting values of $\eta_{\mathrm{t}}k_1^2$ with Re_M is comparable to that of the frequencies found by Käpylä & Brandenburg (2009), but both are about 6 times smaller than those of the nonlinear α^2 dynamo in the present case, where $\tilde{\omega} \approx 1.8\,\mathrm{Re}_\mathrm{M}^{-0.3}$ has been found; cf. Fig. 2. However, for much larger magnetic Reynolds numbers, $\tilde{\omega}$ as well as the growth rate of the large-scale dynamo instability might become independent of Re_M. Interestingly, the normalized growth of the dynamo displays a similar dependence on Re_M; see the lower panel of Fig. 2. Specifically, we find $\tilde{\lambda} \approx 0.0012\,\mathrm{Re}_\mathrm{M}^{-0.38}$.

The cyclic behavior of the dynamo-generated magnetic field is also shown in a series of snapshots in Fig. 3, where we present $\overline{B}_x/B_{\mathrm{eq}}$ in the yz plane at different times. As one can see, dynamo waves propagate toward the surface and the evolution of the polarities is similar.
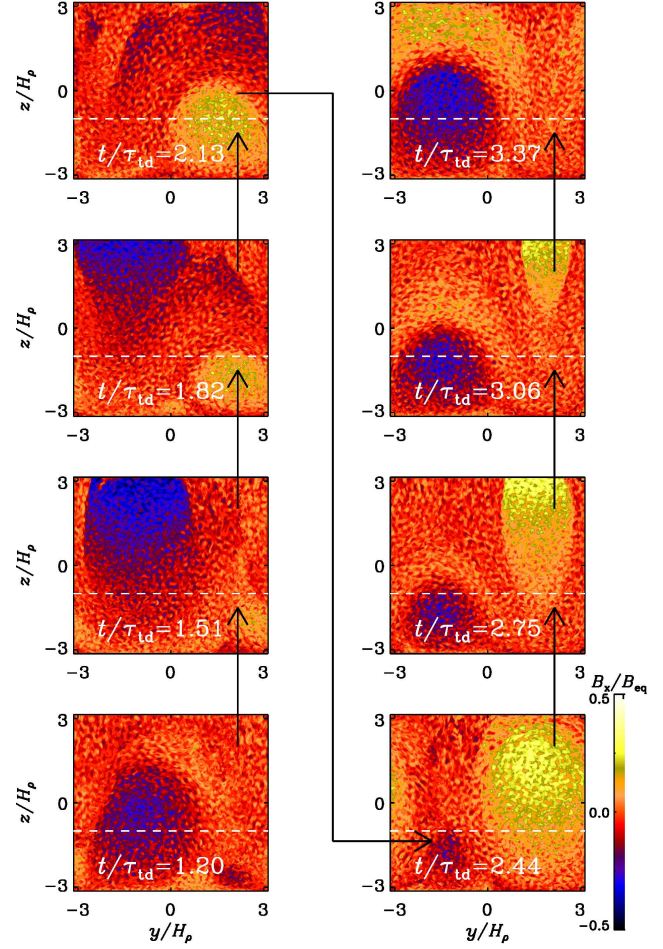
Figure 3. Time evolution of B_x/B_{eq} in the yz plane through $x/H_\rho = \pi$ for Run RM1.

4   MAGNETIC STRUCTURES

As mentioned above, the evolution and formation of the magnetic structures is similar to that of Mitra et al. (2014) and Jabbari et al. (2015). For $\mathrm{Re}_\mathrm{M} = 10$, 16, and 50, bipolar magnetic structures of super-equipartition strength form in about half a turbulent-diffusive time and continue to evolve. For higher Re_M, structures form at later times and survive much longer compared to the case with a smaller Re_M of 10 or 16. However, the type of structures are otherwise similar for all Re_M.

4.1   Production of sharp fronts

In this paper we are interested in the time when structures develop and form "stripy" patterns at the surface (see Figs. 4 and 5). We concentrate on the phase in the evolution when different polarities move close together to form a current sheet between magnetic fields of the opposite polarities. Figure 5 illustrates the time evolution of B_z/B_{eq} at the surface ($z/H_\rho = \pi$). One can see the formation of a sharp boundary between two polarities in the right column, third panel of this figure ($t/\tau_{\mathrm{td}} = 2.75$). It is clear from Fig. 5 that the characteristic time of the formation of the elongated structures is of the order of the period of the dynamo wave, i.e., the turbulent-diffusion time (compare this figure with Fig. 3 for instance).
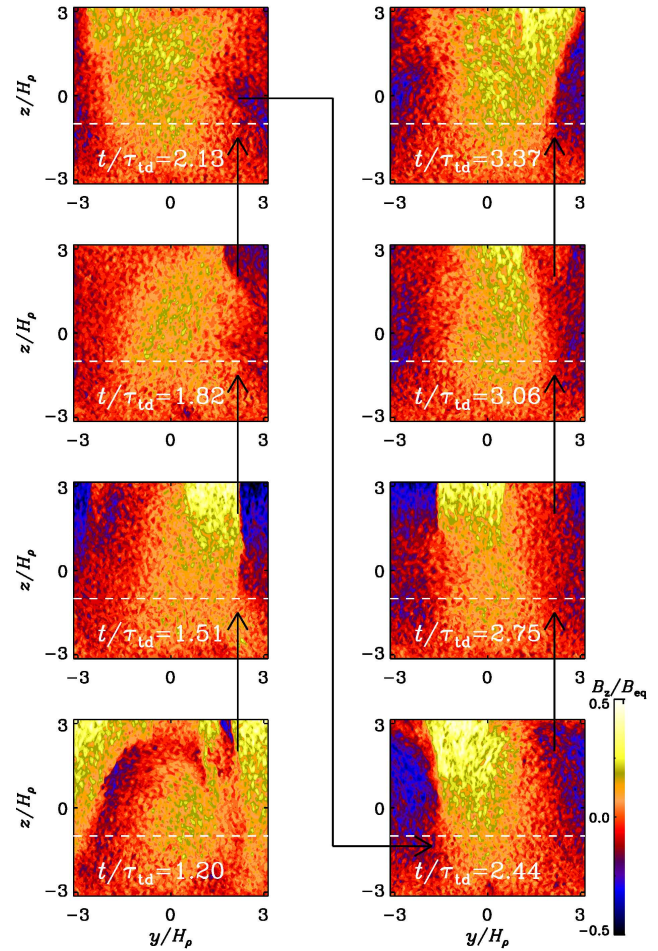
The magnetic surface structures are formed by a redistribution
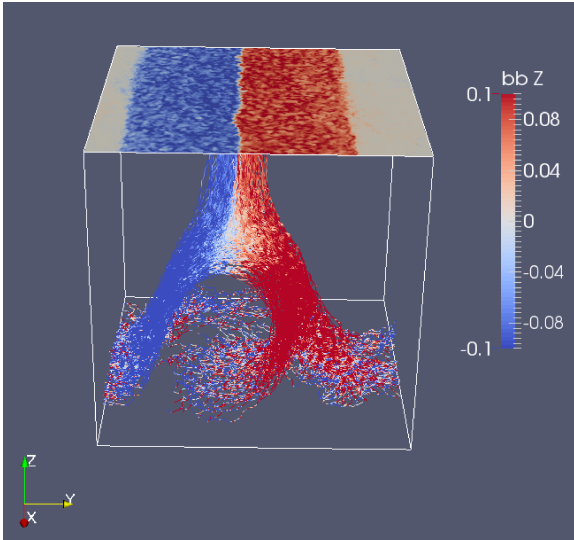
Figure 4. Three-dimensional visualization of vertical magnetic field, B_z at the surface (color-coded) together with three-dimensional volume rendering of the vertical component of the magnetic field for Run RM1.
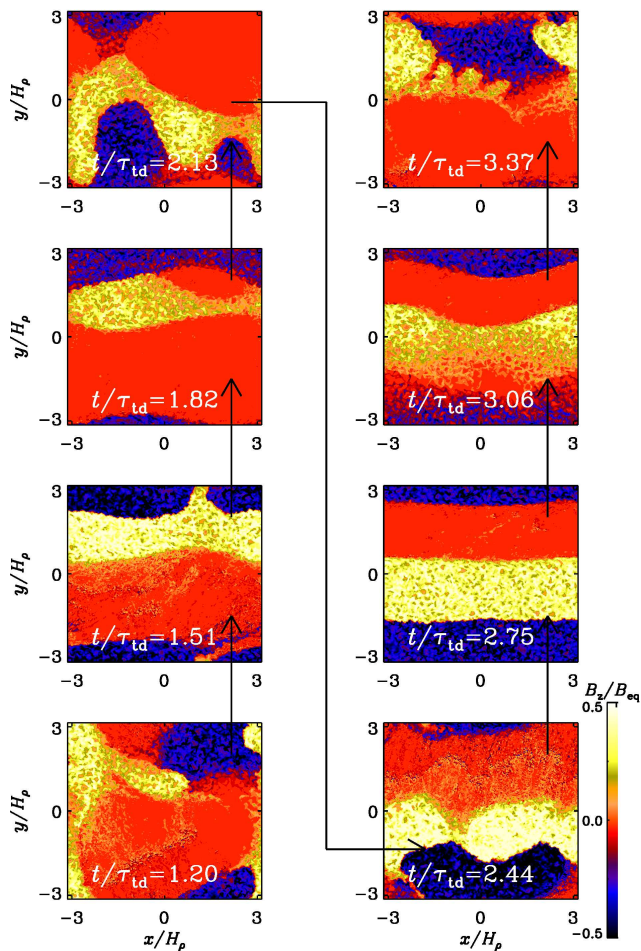
Figure 5. Time evolution of B_z/B_{eq} in the xy plane at the top surface for Run RM1.


Figure 6. Time evolution of B_z/B_{eq} in the yz plane through $x/H_\rho = \pi$ for Run RM1.

of magnetic flux so that regions of highly concentrated magnetic field are separated by regions of low magnetic field. This effect can be seen in Fig. 6 where we show a visualization of B_z/B_{eq} in the same temporal and spatial frame as Fig. 3.

4.2 Relation to downflows

As follows from previous related studies of forced turbulence (Mitra et al. 2014), the magnetic flux concentrations tend to form in regions with downflows. To study this effect we plot in the upper panel of Fig. 7 the large-scale horizontal velocity, $\langle (U_x, U_y) \rangle_{k_6}$ (blue arrows), together with a gray-scale representation of $B_z^2/B_{eq}^2(z)$ at the surface for $t/\tau_{td} = 2.46$. Here, $\langle \cdot \rangle_{k_6}$ denotes Fourier filtering, applied to obtain smoother contours. We see that there are positions where the horizontal velocity around or near the edge of the each spot is high. Furthermore, the horizontal velocity is small where the field is strong, which is consistent with the presence of downflows. This is shown in the lower panel of Fig. 7, where we plot $\langle U_z \rangle_{k_6}$ in an xz plane through $y/H_\rho = -1.5$. There are indeed clear downflows below the magnetic flux concentration. This is in agreement with previous studies of magnetic field concentrations in one-layer turbulence.
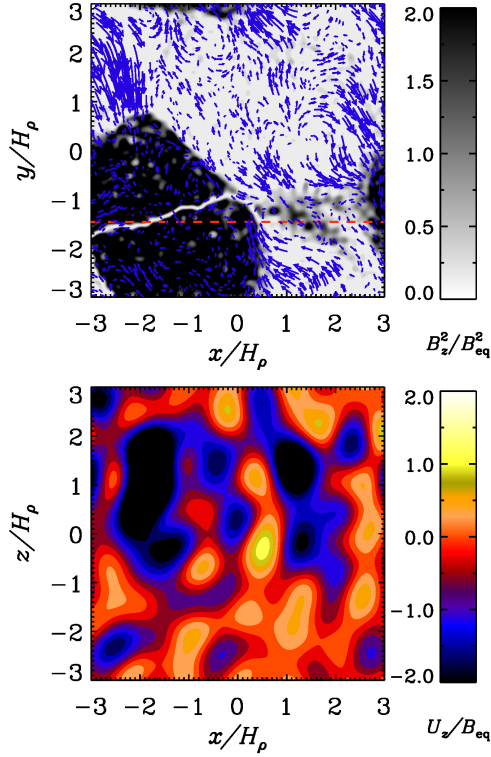
Figure 7. Upper panel: velocity vectors, $\langle U_x \rangle_{k_6}$ and $\langle U_y \rangle_{k_6}$ (blue arrows) plotted on a gray-scale representation of $B_z^2/B_{eq}^2(z)$ at the surface and $t/\tau_{td} = 2.46$ for Run RM1. Lower panel: visualization of $\langle U_z \rangle_{k_6}$ on xz plane at $y/H_\rho = -1.5$ (red dashed line on the upper panel).

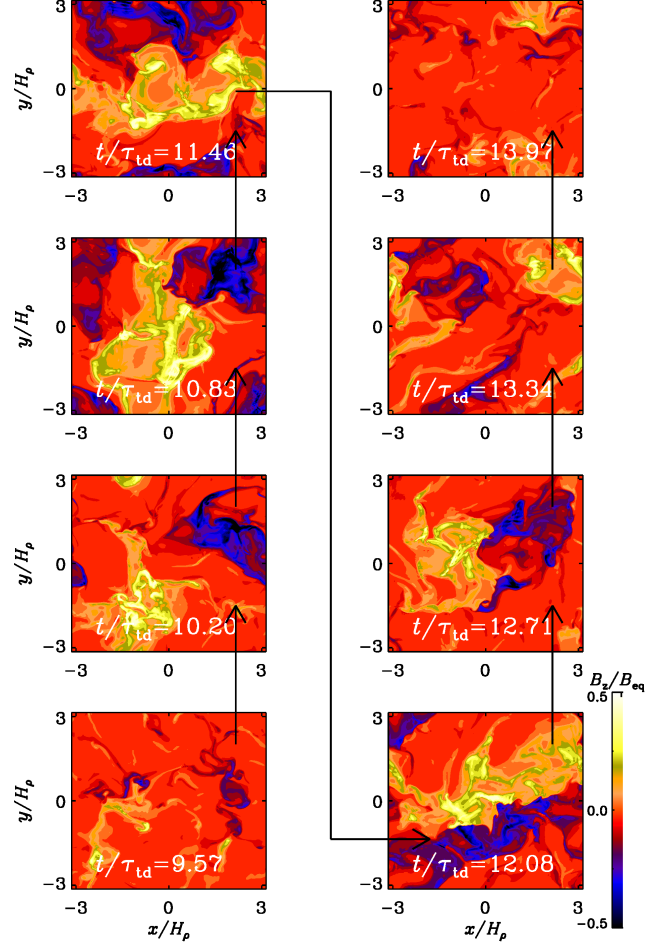**Figure 8.** Same as Fig. 5 but for Run RM1k with $k_f = 5$.

4.3 Scale separation

Previous studies of magnetic flux concentrations in turbulence with weak imposed magnetic field have shown that NEMPI forms magnetic concentrations only when the scale separation ratio, k_f/k_1, is about 15 or larger (Brandenburg et al. 2014). Therefore, we perform a simulation with $k_f/k_1 = 5$ to study whether the formation of structures is still possible in such a model. Figure 8 presents the visualization of B_z at the surface of the box for such a simulation. Surprisingly, in our stratified two-layer forcing model, the bipolar magnetic structures continue to form, and follow a similar evolution as in the case with higher scale separation ratio. The only difference is the time delay in the formation of the first structure and their irregular and fast motions.

The other interesting case is when we apply a forcing profile that is helical in the entire domain (Run RM1zs). In such a system, we expect the formation of a bipolar structure at much earlier times, because the large-scale dynamo is now allowed to work in the entire domain so we should observe propagating dynamo waves at all depths. Our results confirm this already at a time of around $0.37\tau_{td}$, when a magnetic structure develops at the surface and the evolution of the structures occurs faster than in the two-layer simulations.

4.4 Evolution of bipolar structures

To investigate the evolution of the bipolar magnetic structures in more detail, we study the motion in the vicinity of the magnetic structures. In the early stage of the formation of bipolar structures, they tend to have round yin-yang shapes and each polarity rotates

clockwise, independently of each other. When the structures move close enough to each other, their motion is no longer independent. After the formation of the elongated structures (see Fig. 5 at $t/\tau_{td} = 1.51$ and 1.82), one can see an anti-clockwise rotation at the border between opposite polarities (at $t/\tau_{td} = 2.13$ and 2.44 in this figure), which tends to break the connection and destroys the elongated structure. We suggest that the clockwise rotation of structures is due to the presence of a strong large-scale magnetic helicity associated with the structure. In other words, the traveling dynamo waves reach the surface and affect the evolution and motion of the magnetic structures. The anti-clockwise rotation, however, might be driven either by some instability, which occurs when opposite magnetic fields come close to each other (e.g., an instability similar to tearing instability during reconnection) or it might be caused by the interaction of two rotating polarities that are now coupled.

4.5 The effect of rotation

In this work we also study the effect of rotation on the formation and the evolution of the magnetic structures. We perform simulations with different Coriolis numbers, $Co = 0.03$, 0.3, 0.7, and 1.4. Table 2 shows the parameters of these runs. Previous studies showed that for Co larger than 0.1, rotation suppresses the formation of magnetic structures by NEMPI, see Losada et al. (2013) and Jabbari et al. (2014). However, our present study shows that
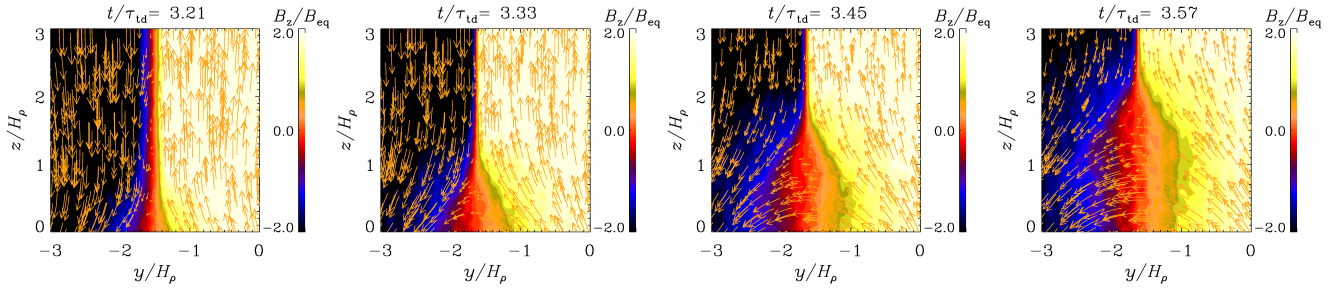
Figure 9. Time evolution of $\overline{B}_z/B_{\rm eq}$, together with $\overline{B}_y/B_{\rm eq}$ and $\overline{B}_z/B_{\rm eq}$ vectors for Run RM1.

Table 2. Summary of the runs with rotation.

| Run	Co	θ	$\lambda/\eta_{\rm t0}k_1^2$
RM1	**0**	**0**	0.0122
R1	0.037	0	0.041
R2	0.37	0	0.040
R3	0.74	0	0.033
R4	0.37	$\pi/4$	0.040
R5	0.37	$\pi/2$	0.040
R6	−0.37	0	0.040
R7	1.4	0	0.015

in our two-layer dynamo model, magnetic structures survive for Co as large as 1.4. It should also be noted that the combination of stratification and rotation leads to the generation of an additional contribution to the kinetic helicity in the system (Krause & Rädler 1980; Kleeorin & Rogachevskii 2003; Jabbari et al. 2014). This contribution is either constructive if Co < 0 (producing extra positive helicity) or destructive if Co > 0 (producing negative helicity). This could modify the dynamo action, but in the present case the Coriolis number is still too small for the rotation-induced helicity to be important; see Fig. 5 of Jabbari et al. (2014).

One of the possible reasons for the existence of magnetic structures for moderate rotation rates (Co ⩽ 1.4) is the large-scale dynamo that increases the magnetic flux. Indeed, NEMPI cannot create a new flux, but can only redistribute it by forming magnetic concentrations in certain small regions. Since the dynamo systematically produces new magnetic flux, and NEMPI redistributes it, the magnetic concentrations survive even for a moderate rotation.

It turns out that in the presence of rotation with Co > 0, there is a delay in the formation of bipolar structures and the development of their shape during the early stage. In the case without rotation, the structure has spherical-like shape in the early stage of formation before it becomes elongated. This does not happen at finite rotation with Co > 0. In the presence of rotation, even in the early stage of bipolar structure formation, it has a random elongated shape, which changes rapidly in time. In the presence of rotation it takes more time for the magnetic structures to become intense and concentrated.

5 RECONNECTION IN THE UPPER LAYERS

The production of sharp fronts can be seen in Figs. 5 and 6, where we plot $\overline{B}_z/B_{\rm eq}$ in two different planes. During the evolution of the magnetic structures, the bipolar regions evolve into stripes of oppo-
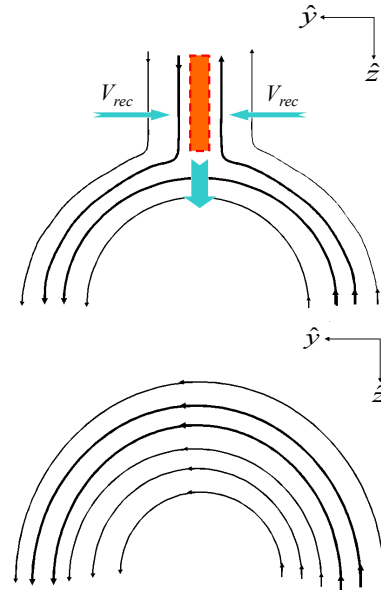
Figure 10. Upper panel: formation of a current sheet before the reconnection. Lower panel: magnetic configuration after the reconnection.

site polarities separated by a current sheet; see Fig. 4. In Fig. 9 we zoom in on the sharp front in $\overline{B}_z/B_{\rm eq}$, where we also see vectors of $\overline{B}_y/B_{\rm eq}$ and $\overline{B}_z/B_{\rm eq}$ in the yz plane for our reference run. By comparing the field lines with Fig. 10, one can see a similar reconfiguration of magnetic field lines during spot evolution. It is clear from this figure that field lines with opposite signs of $\overline{B}_z/B_{\rm eq}$ are reconnected and a y component of the magnetic field is generated.

On a timescale that lies somewhere between the resistive diffusion and Alfvén timescales, magnetic reconnection occurs which causes the magnetic field topology to change and leads to the conversion of magnetic energy to thermal energy, kinetic energy and even particle acceleration; see the sketch in Fig. 10. According to Sweet-Parker theory (Parker 1957; Sweet 1958, 1969; Parker 1994), hereafter SP theory, the rate of reconnection, $V_{\rm rec}$ depends on the Lundquist number, S:

$$V_{\rm rec} = V_{\rm A} S^{-1/2}. \qquad (6)$$

In the turbulent regime of reconnection, $V_{\rm rec}$ is independent of the Ohmic resistivity (Lazarian & Vishniac 1999); see also Eyink et al. (2011). This conclusion is supported by numerical simulations (Kowal et al. 2009). According to Lazarian & Vishniac (1999), the

upper limit for the reconnection rate is:

$$V_{\rm rec} \sim V_{\rm A} M_{\rm A}^2, \qquad (7)$$

where $M_{\rm A} = u_{\rm rms}/V_{\rm A}$ is the Alfvén Mach number.

For large Lundquist numbers, and in the turbulent regime of reconnection, $V_{\rm rec}$ is independent of S. This conclusion is confirmed by recent numerical simulations (Loureiro et al. 2009; Huang & Bhattacharjee 2010). For $S > 10^4$, the Sweet-Parker current sheet is unstable (Biskamp 1986; Loureiro et al. 2005, 2012; Oishi et al. 2015). For spontaneous magnetic reconnection, according to magnetohydrodynamic numerical simulations (Loureiro et al. 2009; Huang & Bhattacharjee 2010; Beresnyak 2013), the rate of the reconnection, $V_{\rm rec}$, for $S > 10^4$ is of the order of

$$V_{\rm rec} \sim (1-3) \times 10^{-2} V_{\rm A}. \qquad (8)$$

To determine $V_{\rm rec}$, one can use two approaches. In one approach, the value of the inflow in the vicinity of the current sheet is measured (as sketched in Fig. 10). For a turbulent plasma, on the other hand, one can use a more general and accurate method. In this approach, one uses Ohm's law:

$$\eta \mu_0 \boldsymbol{J} = \boldsymbol{E} + \boldsymbol{U} \times \boldsymbol{B}, \qquad (9)$$

so that the rate of the reconnection, $V_{\rm rec}$, can be determined as $V_{\rm rec} \simeq V_E$, where

$$V_E = \frac{\langle |\boldsymbol{E}| \rangle}{\langle |\boldsymbol{B}| \rangle} = \frac{\eta \langle |\mu_0 \boldsymbol{J}| \rangle - \langle |\boldsymbol{U} \times \boldsymbol{B}| \rangle}{\langle |\boldsymbol{B}| \rangle}, \qquad (10)$$

and angular brackets denote averaging along the z direction (along the largest side of the current sheet, i.e., perpendicular to the current, see Fig. 10). Thus, the method of the determining $V_{\rm rec}$ in numerical simulations is as follows: (i) find the region with the current sheet that is separating magnetic fields of opposite polarities; (ii) use different instants of the formation of the current sheet and determine the value of $V_{\rm rec}$, the length of the current layer, $\mathcal{L}_z$, in the z direction, the Alfvén speed $V_{\rm A}$ in these instants. Finally, we determine $S^{-1/2}$ and $M_{\rm A}^2 = u_{\rm rms}^2/V_{\rm A}^2$, and compare these quantities with the obtained value of $V_{\rm rec}/V_{\rm A}$. We recall that the length of the current sheet $\mathcal{L}_z$ enters in the definition $S = V_{\rm A} \mathcal{L}_z/\eta$, and the time when $\mathcal{L}_z$ reaches its maximum value marks the starting time of reconnection.

To determine $V_{\rm rec}$ we use x-averaged data, average over the interval (z_1, z_2), where $\mathcal{L}_z = z_2 - z_1$ is the length of the current sheet. Next, we measure the value of $V_{\rm rec}$ as $V_E(y^*)$ and $V_{\rm in}(y^*)$, while y^* is a point, which is in the vicinity of the current sheet. Figure 10, upper panel, already shows the position of $V_{\rm rec}$, which is the same for both $V_{\rm in}$ and V_E.

The resulting values of $V_{\rm rec}$ are summarized in Table 3. For comparison, we measure both the velocity V_E using Eq. (10) and the incoming velocity $V_{\rm in}$ in the vicinity of the current sheet (in the case of a two-dimensional flow in the xz-plane it is in the y direction). We normalize these velocities by $\langle V_{\rm A} \rangle$, because $V_{\rm A}$ varies with time (see Fig. 11). In this section, in order to be able to compare the results of different runs, we use $(t - t_{\rm rec})/\tau_{\rm td}$ for the normalized time, where $t_{\rm rec}$ is the time when the reconnection starts for each individual Run. Figure 11 presents the time evolution of the different quantities in three separate panels: $\langle |\boldsymbol{B}| \rangle$ and $\langle |\boldsymbol{E}| \rangle$ in the upper panel, $V_{\rm A}/\langle V_{\rm A} \rangle$ and $u_{\rm rms}/\langle u_{\rm rms} \rangle$ in the middle panel, and finally $\mathcal{L}_z k_1$ in the lower panel. The different colors represent different values of $\rm Re_M$. One can see that, $u_{\rm rms}/\langle u_{\rm rms} \rangle$ does not change strongly with time and $V_{\rm A}/\langle V_{\rm A} \rangle$ changes when $\rm Re_M$ is smaller ($\rm Re_M = 50$). This implies that the major change in S comes from the change in the length of the current sheet (see the lower panel of Fig. 11).
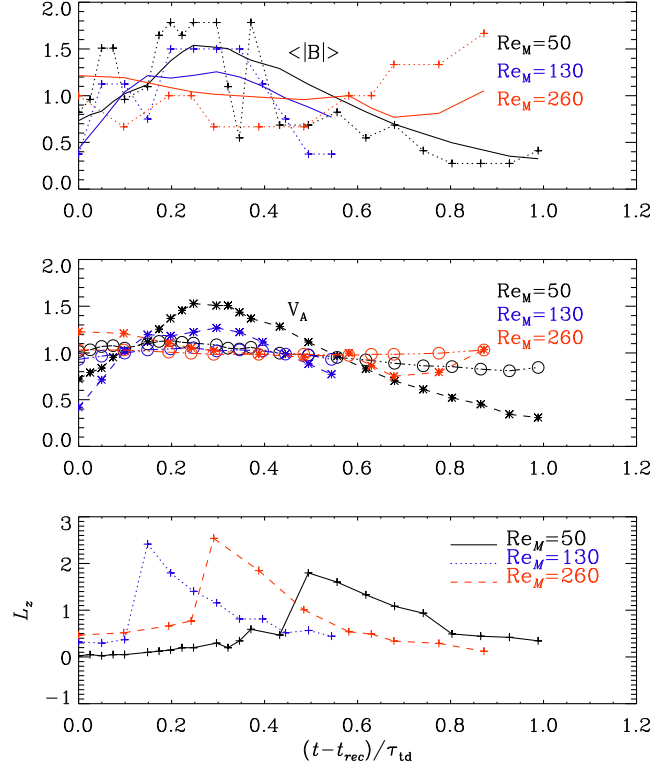
Figure 11. Upper panel: time evolutions of $\langle |\boldsymbol{B}| \rangle$ (solid) and $\langle |\boldsymbol{E}| \rangle$ (dotted), both normalized by their time-averaged value. Different colors are related to three different $\rm Re_M$ (Runs RM1, RM2, and RM3). Middle panel: time evolutions of $V_{\rm A}/\langle V_{\rm A} \rangle$ (stars), and $u_{\rm rms}/\langle u_{\rm rms} \rangle$ (circles) for Runs RM1 (black), RM2 (blue), and RM3 (red). Lower panel: time evolutions of $\mathcal{L}_z k_1$ (triangles) for Runs RM1 (black), RM2 (blue), and RM3 (red).

To check which regime of magnetic reconnection is appropriate, we plot in Fig. 12 V_E as a function of S. By comparing the curves for different magnetic Reynolds numbers, $\rm Re_M = 50, 130, 260$, it is clear that our data points are consistent with the turbulent regime of reconnection (Loureiro et al. 2009; Huang & Bhattacharjee 2010; Loureiro et al. 2012; Beresnyak 2013), where the reconnection rate is nearly independent of S. Fig. 13 demonstrates that the reconnection rates obtained from the measurements of $V_{\rm in}$ and V_E are similar.

The dependence of the reconnection rate on $M_{\rm A}$ is shown in Fig. 14. To compare the resulting data from our simulations with the model of Lazarian & Vishniac (1999), we also plot the linear fit to the data points in Fig. 14. It is clear that our data points strongly deviate from the predicted $M_{\rm A}^2$ line, and are thus inconsistent with Lazarian & Vishniac (1999). However, $V_{\rm rec}$ is weakly dependent on the Ohmic resistivity (see Figs. 12 and 14), in agreement with Lazarian & Vishniac (1999).

6 CONCLUSIONS

In the present paper, we have extended the results of Mitra et al. (2014) to higher magnetic Reynolds numbers and have investigated the effects of rotation at different Coriolis numbers. Our results demonstrate that in the two-layer model with helical forcing in the lower part and non-helical forcing in the upper, sharp bipolar
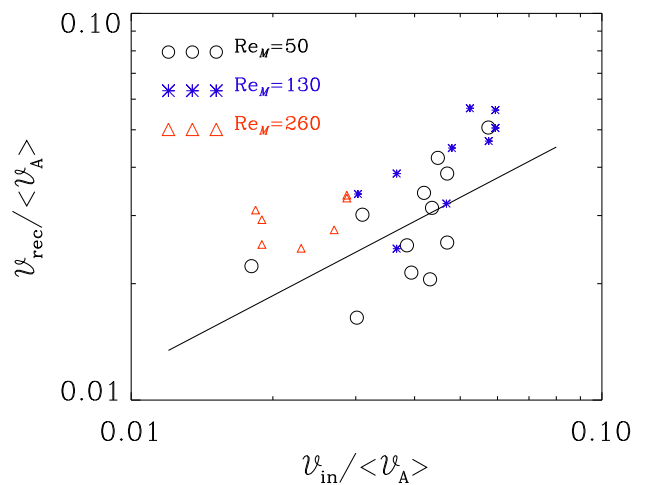
**Table 3.** Summary of the reconnection parameters.

Run	$\mathrm{Re_M}$	η	t/τ_{td}	$\mathcal{L}_z$	$u_{\mathrm{rms}}/c_{\mathrm{s}}$	V_E/c_{s}	V_A/c_{s}	$\mathrm{M_A}$	S	$S^{-1/2}$	V_E/V_A	$\mathrm{M_A^2}$	$V_{\mathrm{in}}/c_{\mathrm{s}}$	V_{in}/V_A
RM0	10	3×10^{-4}	0.97	0.025	0.125	0.04	0.319	0.39	26	0.196	0.127	0.149	0.033	0.104
D1	16	2×10^{-4}	0.65	0.0246	0.12	0.0136	0.231	0.52	28	0.188	0.0589	0.27	0.0101	0.0437
D1	16	2×10^{-4}	0.84	0.0247	0.118	0.0206	0.299	0.4	37	0.165	0.0689	0.156	0.0212	0.0709
D1	16	2×10^{-4}	0.97	0.123	0.104	0.0067	0.169	0.62	104	0.098	0.0397	0.379	0.0075	0.0444
RM1	50	5.7×10^{-5}	2.87	0.0493	0.115	0.0107	0.228	0.5	187	0.073	0.047	0.254	0.0154	0.068
RM1	50	5.7×10^{-5}	2.92	0.0493	0.120	0.0151	0.275	0.44	226	0.067	0.055	0.191	0.0211	0.077
RM1	50	5.7×10^{-5}	2.99	0.0986	0.122	0.0099	0.323	0.38	531	0.043	0.031	0.143	0.0176	0.055
RM1	50	5.7×10^{-5}	3.04	0.1478	0.126	0.0120	0.395	0.32	973	0.032	0.03	0.102	0.0184	0.047
RM1	50	5.7×10^{-5}	3.09	0.1971	0.123	0.0108	0.441	0.28	1449	0.026	0.025	0.078	0.0145	0.033
RM1	50	5.7×10^{-5}	3.16	0.1971	0.117	0.0071	0.435	0.27	1429	0.027	0.016	0.072	0.0093	0.022
RM1	50	5.7×10^{-5}	3.21	0.5914	0.118	0.0121	0.395	0.3	3893	0.016	0.031	0.089	0.0137	0.035
RM1	50	5.7×10^{-5}	3.34	1.7987	0.109	0.0061	0.322	0.34	9653	0.010	0.019	0.115	0.0112	0.035
RM1	50	5.7×10^{-5}	3.46	1.3306	0.103	0.0060	0.239	0.43	5300	0.014	0.025	0.186	0.0092	0.039
RM1	50	5.7×10^{-5}	3.58	0.9363	0.096	0.0075	0.176	0.55	2747	0.019	0.043	0.298	0.0104	0.059
RM1	50	5.7×10^{-5}	3.71	0.4435	0.092	0.0053	0.130	0.71	961	0.032	0.041	0.501	0.0043	0.033
RM1	50	5.7×10^{-5}	3.83	0.3450	0.094	0.0101	0.089	1.06	512	0.044	0.11	1.116	0.0107	0.12
RM2	130	2×10^{-5}	1.6	2.4147	0.092	0.0039	0.183	0.50	22095	0.0067	0.0213	0.253	0.0058	0.032
RM2	130	2×10^{-5}	1.65	1.7987	0.093	0.0089	0.181	0.51	16278	0.0078	0.0492	0.264	0.0094	0.052
RM2	130	2×10^{-5}	1.7	1.4045	0.094	0.0074	0.187	0.50	13132	0.0087	0.0396	0.253	0.0091	0.049
RM2	130	2×10^{-5}	1.75	1.1581	0.091	0.0080	0.194	0.47	11234	0.0094	0.0412	0.220	0.0094	0.049
RM2	130	2×10^{-5}	1.8	0.8131	0.092	0.0080	0.187	0.49	7603	0.0115	0.0428	0.242	0.0094	0.050
RM2	130	2×10^{-5}	1.9	0.5174	0.088	0.0051	0.151	0.58	3906	0.0160	0.0338	0.340	0.0074	0.049
RM3	260	$1. \times 10^{-5}$	3.04	0.468	0.09	0.005	0.198	0.455	9266	0.011	0.024	0.207	0.005	0.024
RM3	260	$1. \times 10^{-5}$	3.24	0.665	0.088	0.006	0.178	0.494	11837	0.009	0.033	0.245	0.005	0.028
RM3	260	$1. \times 10^{-5}$	3.33	2.538	0.086	0.004	0.165	0.521	41877	0.005	0.026	0.272	0.004	0.024
RM3	260	$1. \times 10^{-5}$	3.43	1.848	0.086	0.005	0.159	0.541	29383	0.006	0.032	0.293	0.003	0.021
RM3	260	$1. \times 10^{-5}$	3.53	1.010	0.086	0.006	0.154	0.558	15554	0.008	0.035	0.312	0.003	0.021
RM3	260	$1. \times 10^{-5}$	3.63	0.542	0.087	0.022	0.094	0.926	5094	0.014	0.233	0.857	0.007	0.070
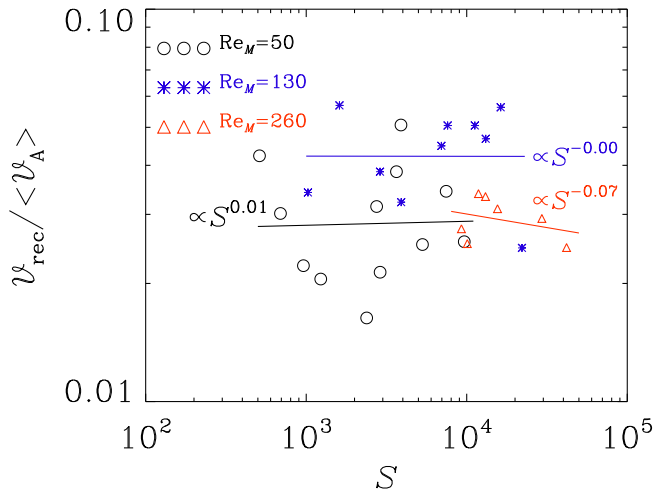
Figure 12. Reconnection rate $V_{\mathrm{E}}/\langle V_{\mathrm{A}}\rangle$ normalized by the mean Alfvén speed versus S. The colors represent the value of $\mathrm{Re_M}$ (Runs RM1 (circles), RM2 (stars), and RM3 (triangles)).

Figure 13. Reconnection rate $V_{\mathrm{E}}/\langle V_{\mathrm{A}}\rangle$ normalized by the mean Alfvén speed versus $V_{\mathrm{in}}/\langle V_{\mathrm{A}}\rangle$. The colors represent the value of $\mathrm{Re_M}$ (Runs RM1 (circles), RM2 (stars), and RM3 (triangles)).

spots form at the surface, expand and then develop stripy structures. The observed effects are similar for different values of $\mathrm{Re_M}$ and Co. In our present simulations, for Co as large as 1.4, we still observe the formation of the intense bipolar structures. This value is significantly larger than what was previously obtained in studies of magnetic flux concentrations in rotating turbulence with an imposed weak magnetic field. One of the plausible explanations for this is the large-scale dynamo which increases magnetic flux. By

contrast, NEMPI cannot produce new flux, but only redistribute it, forming magnetic concentrations in small regions. Thus, the large-scale dynamo systematically produces new magnetic flux, while NEMPI redistributes it. This could be the reason why the magnetic concentrations survive even for moderate rotation. Although there are dynamo-generated magnetic fields in our simulations, which is more realistic compared to several previous models with an imposed magnetic field, we still observe evidence for downflows at
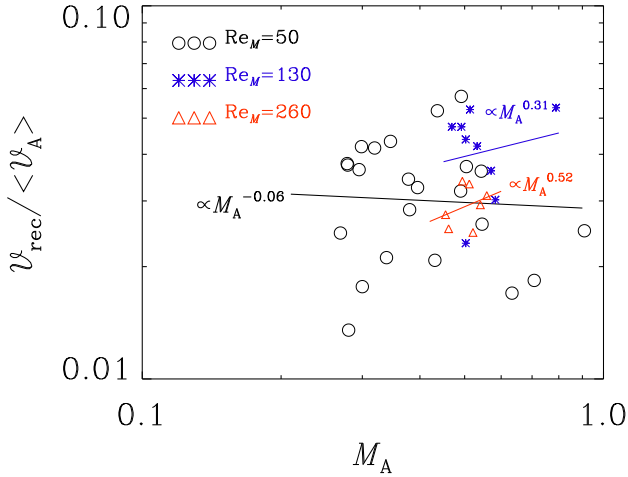
Figure 14. V_E normalized by $\langle V_A \rangle$ as a function of M_A. The solid line presents the best linear fit. Different colors present different values of Re_M ($Re_M=50$ (Run RM1), black circles, $Re_M=130$ (Run RM2), blue stars, and $Re_M=260$ (Run RM3), red triangles).

the locations of magnetic structure formation, similar to Brandenburg et al. (2014), Mitra et al. (2014), and Jabbari et al. (2015).

What is surprising is the long lifetime of the resulting bipolar regions, which exceeds several turbulent diffusion times. We suggest that the main reason why these intense magnetic structures survive longer is the magnetic reconnection phenomenon in the vicinity of the current sheet between opposite magnetic polarities. We have determined the reconnection rate for a range of different parameters and have shown that for high Lundquist numbers, $S > 10^3$, the measured reconnection rate is nearly independent of S. This result is consistent with recent numerical simulations in a turbulent regime of reconnection performed by other groups (Loureiro et al. 2009; Huang & Bhattacharjee 2010; Loureiro et al. 2012; Beresnyak 2013). The measured reconnection rate is weakly dependent on the Alfvén Mach number, M_A^2, which is inconsistent with predictions of Lazarian & Vishniac (1999). On the other hand, the reconnection rate is also weakly dependent on the Ohmic resistivity, in agreement with Lazarian & Vishniac (1999).

In the present work, we have also investigated the effects of varying the scale separation ratio, k_f/k_1. Contrary to earlier studies of NEMPI, for k_f/k_1 as small as five, bipolar magnetic structures still form. Our previous studies of an unipolar magnetic concentrations with an imposed weak mean magnetic field have shown that, although the effective magnetic pressure (the sum of turbulent and non-turbulent contributions) becomes negative even for moderate scale separation ratio (about 3–5), the large-scale instability (NEMPI) is excited only if the scale separation ratio is large enough (> 15). This suggests that the phenomenon we find in our DNS cannot be understood solely in terms of NEMPI.

In the more complicated two-layer system with a dynamo-generated magnetic field, two instabilities (dynamo and possibly NEMPI or the magnetic buoyancy instability) may be excited. We stress that in both, our two-layer model with dynamo-generated magnetic field and in turbulent systems with an imposed magnetic field where NEMPI is known to be excited, strong density stratification plays an important role. Furthermore, there is evidence for the existence of downflows at the locations of magnetic structures in both systems. However, in our two-layer model the formation of bipolar regions is still observed for smaller scale separation ra-

tios than what was required for a turbulent system with an imposed magnetic field where NEMPI was excited.

The process maintaining the bipolar structures may be related to or associated with NEMPI. It may also be possible that the positive magnetic pressure associated with the strong dynamo-generated magnetic field in nonlinear stage of evolution is responsible for the formation of the sharp interface of the bipolar structures found in the upper layers, where the plasma beta is no longer very large. However, a conclusive answer cannot be given at present. To arrive at a more definitive conclusion regarding the mechanism of bipolar structure formation, it would be desirable to measure the effective magnetic pressure tensors in our two-layer model and to study their parameter dependencies in more detail. This requires the development of an adequate test-field method. This is a subject of a separate study.

REFERENCES

Beresnyak, A. 2013, arXiv: 1301.7424.

Biskamp, D. 1986, Phys. Fluids, 29, 1520

Brandenburg, A., Gressel, O., Jabbari, S., Kleeorin, N., & Rogachevskii, I. 2014, A&A, 562, A53

Brandenburg, A., Kemel, K., Kleeorin, N., Mitra, D., Rogachevskii, I. 2011, ApJ, 740, L50

Brandenburg, A., Kemel, K., Kleeorin, N., Rogachevskii, I. 2012, ApJ, 749, 179

Brandenburg, A., Kleeorin, N., & Rogachevskii, I. 2010, Astron. Nachr., 331, 5

Brandenburg, A., Kleeorin, N., & Rogachevskii, I. 2013, ApJ, 776, L23

Brandenburg, A., Rädler, K.-H., Rheinhardt, M., & Subramanian, K. 2008, ApJ, 687, L49

Choudhuri, A. R., Schüssler, M., & Dikpati, M. 1995, A&A, 303, L29

D'Silva, S., & Choudhuri, A. R. 1993, A&A, 272, 621

Eyink, G. L., Lazarian, A. & Vishniac E. T. 2011, ApJ, 743, 51

Fan, Y. 2009, Living Rev. Solar Phys., 6, 4

Getling, A. V., Ishikawa, R., & Buchnev, A. A. 2016, Solar Phys., 291, 371

Guerrero, G. & Käpylä, P. J. 2011, A&A, 533, A40

Huang, Y.-M. & Bhattacharjee, A. 2010, Phys. Plasmas, 17, 062104

Jabbari, S., Brandenburg, A., Kleeorin, N., Mitra, D., & Rogachevskii, I. 2013, A&A, 556, A106

Jabbari, S., Brandenburg, A., Losada, I. R., Kleeorin, N., & Rogachevskii, I. 2014, A&A, 568, A112

Jabbari, S., Brandenburg, A., Kleeorin, N., Mitra, D.,& Rogachevskii, I. 2015, ApJ, 805, 166

Käpylä, P. J., & Brandenburg, A. 2009, ApJ, 699, 1059

Käpylä, P. J., Brandenburg, A., Kleeorin, N., Mantere, M. J., & Rogachevskii, I. 2012, MNRAS, 422, 2465

Käpylä, P. J., Brandenburg, A., Kleeorin, N., Käpylä, M. J., & Rogachevskii, I. 2016, A&A, 588, A150

Kemel, K., Brandenburg, A., Kleeorin, N., Mitra, D., & Rogachevskii, I. 2013, Solar Phys., 287, 293

Kleeorin, N., Mond, M., & Rogachevskii, I. 1993, Phys. Fluids B, 5, 4128

Kleeorin, N., Mond, M., & Rogachevskii, I. 1996, A&A, 307, 293

Kleeorin, N., & Rogachevskii, I. 1994, Phys. Rev. E, 50, 2716

Kleeorin, N., & Rogachevskii, I. 2003, Phys. Rev. E, 67, 026321

Kleeorin, N.I., Rogachevskii, I.V., & Ruzmaikin, A.A. 1989, Sov. Astron. Lett., 15, 274

Kleeorin, N. I., Rogachevskii, I. V., Ruzmaikin, A. A. 1990, Sov. Phys. JETP, 70, 878

Kowal, G., Lazarian, A., Vishniac E. T., & Otmianowska-Mazur, K. 2009, ApJ, 700, 63

Krause F., Rädler K.-H., 1980, Mean-Field Magnetohydrodynamics and Dynamo Theory. Pergamon, Oxford

Krivodubskii, V. N. 1984, Sov. Astron., 28, 205

Lazarian, A. & Vishniac E. T. 1999, ApJ, 517, 700

Lazarian, A., Eyink, G. L., Vishniac, E. T., & Kowal, G. 2015, Phil. Trans. Roy. Soc. A, 373, 20140144

Losada, I. R., Brandenburg, A., Kleeorin, N., & Rogachevskii, I. 2013, A&A, 556, A83

Loureiro, N. F., Cowley, S. C., Dorland, W. D., Haines, M. G. Schekochihin, A. A. 2005, Phys. Rev. Lett., 95, 235003

Loureiro, N. F., Uzdensky, D. A., Schekochihin, A. A., Cowley, S. C., Yousef, T. A. 2009, MNRAS, 399, L146

Loureiro, N. F., Samtaney, R., Schekochihin, A. A. & Uzdensky, D. A. 2012, Phys. Plasmas, 19, 042303

Loureiro, N. F., Schekochihin, A. A., & Uzdensky, D. A. 2013, Phys. Rev. E, 87, 013102

Mitra, D., Brandenburg, A., Kleeorin, N., & Rogachevskii, I. 2014, MNRAS, 445, 761

Oishi, J. S., Mac Low, M.-M., Collins, D. C., & Tamura, M. 2015, ApJ, 806, L12

Parker, E. N. 1955, ApJ, 121, 491

Parker, E. N. 1957, J. Geophys. Res., 62, 509

Parker, E. N., Spontaneous current sheets in magnetic fields: with applications to stellar x-rays (Oxford University Press, USA, 1994)

Priest, E., Magnetohydrodynamics of the Sun (Cambridge University Press, New York, 2014)

Rogachevskii, I., & Kleeorin, N. 2007, Phys. Rev. E, 76, 056307

Sweet, P. A., Proc. IAU Symp. no. 6., p. 123 (1958).

Sweet, P. A. 1969, ARA&A, 7, 149

Uzdensky, D. A., Loureiro, N. F., Schekochihin, A. A. 2010, Phys. Rev. Lett., 105, 235002

Warnecke, J., Losada, I. R., Brandenburg, A., Kleeorin, N., & Rogachevskii, I. 2013, ApJ, 777, L37

Warnecke, J., Losada, I. R., Brandenburg, A., Kleeorin, N., & Rogachevskii, I. 2016, A&A, in press, arXiv:1502.03799

Zhao, J., Bogart, R. S., Kosovichev, A. G., Duvall, Jr., T. L., & Hartlep, T. 2013, ApJ, 774, L29

Zweibel, E. G., & Yamada, M. 2009, ARA&A, 47, 291